ORIGINAL ARTICLE

The East Asian Summer Monsoon Response to Global Warming in a High Resolution Coupled Model: Mean and Extremes

Zhen Liu[1,2] · Sun-Seon Lee[1,2] · Arjun Babu Nellikkattil[1,2] · June-Yi Lee[1,3,4] · Lan Dai[1,2] · Kyung-Ja Ha[1,3,4,5] · Christian L. E. Franzke[1,2]

Abstract

Current climate models still have considerable biases in the simulation of the East Asian summer monsoon (EASM), which in turn reduces their reliability of monsoon projections under global warming. We hypothesize that a higher-resolution coupled climate model with atmospheric and oceanic components at horizontal resolutions of 0.25° and 0.1°, respectively, will better capture regional details and extremes of the EASM. Present-day (PD), $2 \times CO_2$ and $4 \times CO_2$ simulations are conducted with the Community Earth System Model (CESM1.2.2) to evaluate PD simulation performance and quantify future changes. Indeed, our PD simulation well reproduces the climatological seasonal mean and intra-seasonal northward advancement of the monsoon rainband, as well as climate extremes. Compared with the PD simulation, the perturbed CO_2 experiments show an intensified EASM response to CO_2-induced warming. We find that the precipitation increases of the Meiyu-Baiu-Changma band are caused by comparable contributions from the dynamical and thermodynamical components in $2 \times CO_2$, while they are more driven by the thermodynamical component in $4 \times CO_2$ due to stronger upper atmospheric stability. The regional changes in the probability distribution of the temperature show that extreme temperatures warm faster than the most often temperatures, increasing the skewness. Fitting extreme precipitation values with a generalized Pareto distribution model reveals that they increase significantly in $4 \times CO_2$. Changes of temperature extremes scale with the CO_2 concentrations over the monsoon domain but not for precipitation extreme changes. The 99th percentile of precipitation over the monsoon region increases at a super Clausius-Clapeyron rate, $\sim 8\% \ K^{-1}$, which is mainly caused by increased moisture transport through anomalous southerly winds.

Keywords East Asian summer monsoon · High resolution coupled model · CESM · Global warming · Climate extremes

✉ Christian L. E. Franzke
christian.franzke@pusan.ac.kr

1. Center for Climate Physics, Institute for Basic Science, Busan, Republic of Korea

2. Pusan National University, Busan, Republic of Korea

3. Department of Climate System, Pusan National University, Busan, Republic of Korea

4. Research Center for Climate Sciences, Pusan National University, Busan, Republic of Korea

5. BK21 School of Earth and Environmental Systems, Pusan National University, Busan, Republic of Korea

1 Introduction

The East Asian summer monsoon (EASM) is one of the most vibrant climate system components, encompassing a large spatial coverage and a wide range of time scales. Its seasonal evolution is characterized by the northwestward movement of a zonally elongated Meiyu-Baiu-Changma rainband strongly modulated by the western Pacific subtropical high (WPSH) and the dynamical effect of the Tibetan Plateau, providing water resources for one third of the world's population (e.g., Lau and Ploshay 2009; Son et al. 2019, 2020; Oh and Ha 2020; Son and Seo 2022). Furthermore, climate extremes (e.g., heatwaves and floods) are closely linked to variations in the EASM, which pose severe threats to human lives and property (Zhou et al. 2013; Zhou and Zou 2014; Wilcox et al. 2015; Lee et al. 2017).

Numerical models have proven to be powerful tools in reproducing the basic structure of the monsoon circulation and precipitation (Lau and Ploshay 2009; Xin et al. 2020; Sperber et al. 2013). However, some model biases, such as the monsoon precipitation distribution (Huang et al. 2013), seasonal evolution (Zou and Zhou 2015), and associated climate extremes (Chen et al. 2021) on different time scales, have persisted for decades. These biases possibly result from the unrealistic representation of physical processes (e.g., convection, Liu et al., 2021) and of complex terrain effects (Boos and Hurley 2013; Lee et al. 2015). Previous studies suggested that increasing the model resolution can considerably improve the monsoon performance in both atmosphere-only (e.g., Kitoh and Kusunoki, 2008) and coupled models (e.g., Yao et al. 2017; Chen et al. 2021).

Most global monsoon systems are projected to have a weakened circulation and enhanced precipitation in the Northern Hemisphere under global warming (Lee et al., 2021). Besides the humidity increase, greenhouse gas warming generally affects the monsoon dynamically in two contrasting ways (Seo et al. 2013; Lee and Wang 2014; Wang et al. 2020; Moon and Ha, 2020). On one hand, due to relatively larger temperature increases in the upper atmosphere, increased atmospheric stability suppresses convection and precipitation. On the other hand, increasing greenhouse gases induce a land-sea contrast and can act oppositely on different time scales (Shaw and Voigt 2015; Chen and Bordoni 2016). The fast responses due to a reduction of radiative forcing in the absence of sea-surface temperature (SST) changes cause land to warm faster than the ocean, intensifying the WPSH and enhancing the inland moisture transport and subsequent convergence and precipitation increases (Li et al. 2019). On longer time scales, the subsequent SST warming weakens the land-sea thermal contrast, resulting in decreases in monsoon rainfall and circulation (Chen and Bordoni 2016). Despite its important role, the dynamic response of the EASM to CO_2-induced warming is still largely uncertain, poorly understood and warrants further investigation (Wang et al. 2020; Zhou et al. 2018). Chen et al. (2018) reported an underestimation of future Meiyu rainfall changes under global warming in coarse resolution models due to a too weak southwesterly response associated with an eastward shift of WPSH. They claimed that increasing model resolution to resolve complex terrain and parameterizations is essential to reduce uncertainties in the projection of EASM changes. Moreover, higher resolution models are also found superior to relatively lower resolution models in simulating precipitation extremes (Iles et al. 2020; Chen et al. 2021) as well as their projections in responses to CO_2 forcing (van der Wiel et al., 2016). This conclusion is also applied to models including air-sea interactions compared to atmosphere-only simulations (Fischer et al. 2018; Kim et al. 2021).

In this study, we used data from coupled experiments with one of the highest atmospheric and oceanic resolutions performed so far, to evaluate its performance on EASM and their responses to different CO_2 concentration levels across various time scales. We show that these high resolution coupled simulations produce better performances and projections of the monsoon, as well as advance our understanding of physical mechanism in CO_2-forced monsoon changes. The model experimental design and analysis method are documented in Section 2. Results are described in Section 3. Finally, main conclusions are given in Section 4.

2 Data and Methods

2.1 Model and Observation-Based Data

We use three century-long simulations of the Community Earth System Model (CESM) version 1.2.2. The horizontal resolutions of atmospheric and oceanic components are around 0.25° and 0.1°, respectively, ranking among the finest resolved coupled model simulations conducted up to now. The present-day simulation (PD) is run for 140 years with a CO_2 concentration level of 367 ppm corresponding to the Year 2000 condition in as Small et al. (2014). This level enables us to make comparisons with recent-era climatology but note that differences may potentially come from the constant forcing used when comparing with transient reanalysis. From year 71 of the PD simulation, two new simulations were spun up, where the CO_2 concentrations were increased to 2 times (734 ppm; $2 \times CO_2$) and 4 times (1468 ppm; $4 \times CO_2$), and run for 100 years for each experiment. The details of the model set up have been documented in Chu et al. (2020) and Huang et al. (2021). Only results based on the last 40-years, after the simulations reached near-equilibrium as shown in the timeseries of global surface temperature, radiative forcing at the top of atmosphere (see Fig. S1 in Chu et al., 2020), and intensity of the WPSH and EASM (Fig. S1), are analyzed. In contrast to lower resolution simulations, the PD experiment shows considerable improvements in the annual-mean spatial distribution of precipitation and SST (Chu et al. 2020), which may substantially improve the projected SST warming and land-sea contrast. Besides, the high resolution coupled simulation is also expected to resolve the local terrain effect (e.g., the Maritime Continent; Chang et al., 2016; Yamanaka et al., 2018) well and, thus, to improve the monsoon representation (e.g., Liu et al., 2021). This improved air-sea interaction is critical to simulating the land-sea thermal contrast and subsequent monsoon circulation (Wang et al. 2005). With these experiments, we evaluate how these high resolution coupled simulations replicate the EASM and investigate its response

to CO_2 forcing by examining the differences between perturbed CO_2 and the PD simulations.

The seasonal mean in summer (June–August) and intraseasonal features on pentad scales are evaluated against observations at a horizontal resolution of around 25 km. For evaluating the simulation quality of precipitation, we choose the Asian Precipitation-Highly Resolved Observational Data Integration Towards Evaluation of Water Resources (APHRODITE; Yatagai et al. 2012) dataset during 1976 to 2015, the Tropical Rainfall Measuring Mission (TRMM; Huffman et al., 2007) during 1998 to 2019, and the ECMWF fifth generation reanalysis (ERA5; Hersbach et al., 2020) during 1981 to 2020 for daily precipitation. The simulated temperature field is assessed against APHRODITE and ERA5 reanalysis, and the latter is also used to evaluate the simulated large-scale circulation.

2.2 Analysis Methods

To disentangle the contribution of circulation and humidity changes accounting for precipitation changes, the moisture budget is analyzed by decomposing the moisture flux convergence (MFC) as in Seager et al. (2010) and D'Agostino et al. (2019). The changes of precipitation minus evaporation (P – E) should approximately be equal to changes of the vertically integrated MFC:

$$\rho_w g \delta(P - E) \cong \delta MFC \cong -\int_{p_t}^{p_s} \nabla \bullet (\overline{q} \delta \overline{u}) dp - \int_{p_t}^{p_s} \nabla \bullet (\overline{u} \delta \overline{q}) dp - \int_{p_t}^{p_s} \nabla \bullet \delta(\overline{u'q'}) dp - \delta S$$

Here ρ_w is the water density, g is the gravitational constant, p_s is the surface pressure, p_t is the top pressure (i.e., 10 hPa), **u** is the horizontal wind, q is the specific humidity, and S is the surface quantity related to moisture transport by surface flow, which is usually small and not further discussed here. The overbar denotes the monthly mean, and the prime represents daily anomalies relative to the monthly mean. Thus, the first and second terms on the right-hand side represent the monthly moisture transport changes by the dynamical (DY) and thermodynamical (TH) components, respectively. The third term denotes the contribution from transient eddies on time scales less than one month. We checked that the quadratic term (e.g., $\int_{p_t}^{p_s} \nabla \bullet (\delta \overline{u} \delta \overline{q}) dp$) is small and, similar to Oh et al. (2018), we neglected it.

The monsoon onset and withdrawal dates are defined as the first and last pentad of the rainy season, respectively, whose rainfall amount exceeds and drops below the January mean precipitation by 5 mm/day over the monsoon domain (Wang and Ho 2002). The monsoon domain refers to the region where the differences between maximum pentad precipitation and January mean precipitation are larger than 5 mm/day during the extended summer (May–September).

Two extreme climate indices, the 95th and 99th percentile of daily near-surface air temperature (T95 and T99) and precipitation (R95 and R99) are analyzed in this study. The generalized Pareto distribution (GPD) is used to model the exceedances over a precipitation threshold (Coles 2001). Comparing the shape and scale parameters of the distribution in different experiments helps us to identify whether the changes of extreme precipitation are significant or not. The significance of the spatial distribution of the differences between increased CO_2 runs and the PD simulation is estimated by the Student's *t* test. The non-parametric Kolmogorov test is adopted to assess the significance of the probability density distribution differences between the CO_2 perturbed and PD simulations.

3 Results

3.1 Evaluation of Present-Day Simulation

Figure 1 shows the distribution of the climatological summer mean precipitation and 850-hPa wind in observations and the PD simulation. The precipitation pattern is characterized by its maxima on the windward side of the high terrain continent over the western edge of India, Indochina and the nearby Bay of Bengal, and the Philippines, along the Himalayas, and over the western tropical Pacific, South Korea, and southern Japan. The PD simulation overestimates the precipitation over the Himalaya as does the ERA5 reanalysis. This is consistent with previous CESM simulations (e.g., Palazzi et al. 2015). Over the tropical regions, the simulated westerly winds are much weaker over the Bay of Bengal and the South China Sea compared with those in the ERA5 reanalysis. As a result, the precipitation deficit appears over the west coast of Indochina and the Philippines and surrounding oceans to their west, while excessive precipitation occurs in the western Bay of Bengal and the South China Sea, exhibiting a zonal dipolar pattern of biases. Chen et al. (2019) reported a similar finding in a multiyear 3-day hindcast simulation with a well-constrained synoptic scale circulation, and thus attributed the biases to local circulation errors associated with fast physical processes (e.g., convection and the diurnal cycle). Another possible reason could be that a resolution of 25 km still cannot resolve local terrain peaks, leading to a weak blocking effect and less precipitation on the windward side (e.g. the Arakan Mountains in Indochina; Wu et al. 2014). These dry biases near the western coast of Indochina and the Philippines generate weaker low-level convergence and westerly winds as a positive feedback. Consequently, the tropical westerlies easily turn northward toward South China, showing a stronger EASM circulation and precipitation in the PD than the observations. Meanwhile, the WPSH is stronger in

Fig. 1 The spatial distribution of climatological precipitation (mm/day) and 850-hPa wind (m/s) in summer (June–August). Results are based on (**a**) APHRODITE from 1976 to 2015, (**b**) TRMM from 1998 to 2019, (**c**) ERA5 reanalysis from 1981 to 2020, (**d**) present-day (PD) simulation from the Year 101 to Year 140. The numbers in the parenthesis denote the pattern correlation of precipitation between observations and PD


Precip and 850-hPa wind (JJA)

(a) APHRODITE (0.77) (c) ERA5 (0.84) 6 m s⁻¹

(b) TRMM (0.74) (d) PD

[mm/day]
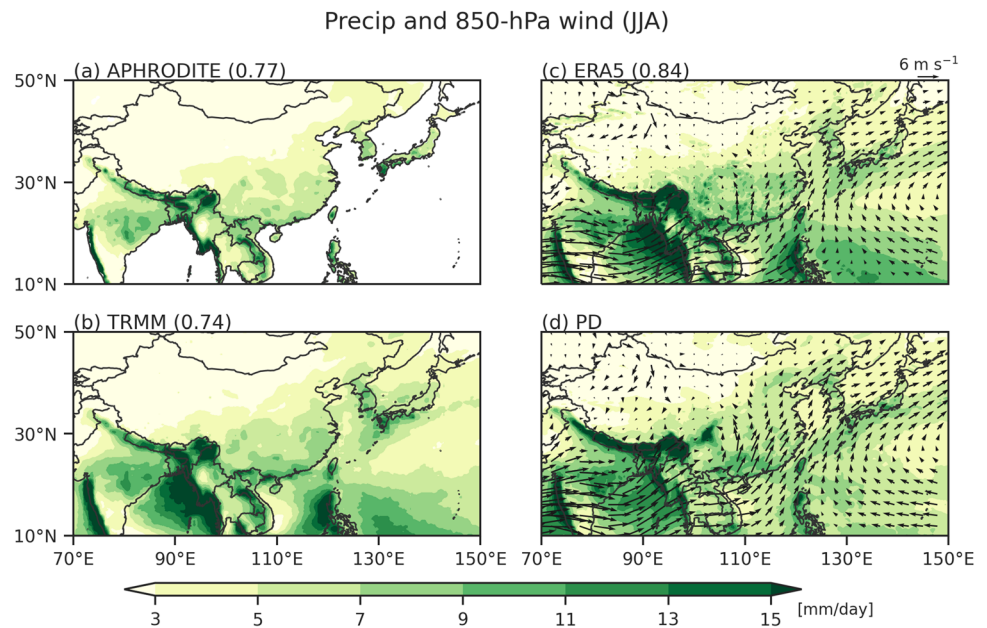
PD than ERA5 as manifested by the excessively strong tropical easterly winds reaching at around 125°E compared to 130°E in the latter, resulting in dry biases over the western tropical Pacific and a stronger monsoon circulation. We note that most of the coupled models in the Coupled Model Intercomparison Project Phase 6 (CMIP6) archive tend to underestimate the EASM precipitation associated with a weaker WPSH and monsoon circulation than observations (Wang et al. 2020; Fig. S7 in Wilcox et al., 2020).Whereas discrepancies are present in the PD, the model well replicates the distribution of the observed seasonal mean precipitation and 850-hPa wind, with spatial correlation coefficients of precipitation above 0.70 (statistically significant at the 1% level). Therefore, our high resolution coupled simulation can reproduce well the seasonal mean features of the EASM circulation and precipitation.

The intra-seasonal evolution of the EASM is accompanied by a northward advancement of an elongated rain belt following the northward movement of the WPSH from early June to mid-July (Ding 1992; Wang and Ho 2002; Chu et al. 2017). During the 31 May–9 June period, the heavy rainband extends from South China to the southern tip of Japan (Fig. 2a and e). This rain belt intensifies and reaches the Yangtze River basin and southern Japan in the following two pentads associated with enhanced WPSH and southerly winds coming from the eastern Bay of Bengal and the South China Sea (Fig. 2b and f). By the end of June, the intense precipitation zone is situated at central China stretching northeastward to central Japan together with the northward shift of the WPSH (Fig. 2c and g). Then the WPSH moves further north but with slightly weakened southwesterly winds on its northwestern flank during early July (Fig. 2d and h). The rainfall belt covers South Korea

and most of Japan and becomes weaker. The model well reproduces the slanted and elongated rainfall belt and its stepwise northward advancement associated with the WPSH northward shift, although the monsoon arrival date is about 2 pentads earlier than observed (Fig. 2i–l). This finding is similar to that reported in Lau and Ploshay (2009) using an atmospheric general circulation model at a resolution of around 50 km. However, our PD simulation produces a much closer match in magnitude and pattern of rainfall to observations than their results. Inspection of the low-level circulation shows that the earlier onset of the rainy season in the simulation is likely induced by the too strong southerly wind over East Asia. The excessively powerful monsoon circulation originates mainly from the excessively strong southerly wind coming from the Bay of Bengal, the South China Sea, and the western tropical Pacific associated with dry biases there. The precipitation and low-level circulation biases on the intra-seasonal scale resemble those on the seasonal mean scale suggesting a common cause for these biases as discussed before.

Extreme weather and climate phenomena are closely linked with variations of the large-scale circulation patterns over Asia during the monsoon season (e.g., Chen and Zhai 2014; Luo and Lau 2017). The patterns of T95 and T99 are very similar, with higher temperature over the land than the ocean (Fig. 3a, b, d and e), particularly over northern India and central eastern China where a strong monsoon circulation occurs. The PD experiment generally overestimates the temperature extremes, especially over warm areas (Fig. 3c and f). Despite this overestimation, the model well captures the pattern of temperature extremes over Asia with a pattern correlation of about 0.95 (statistically significant

Fig. 2 The spatial distribution of climatological precipitation (mm/day) in TRMM for the (**a**) period 1 (P1; 31 May–9 Jun), (**b**) P2 (10 Jun–19 Jun), (**c**) P3 (20 Jun–29 Jun), and (**d**) P4(30 Jun–9 Jul). (**e–h**), (**i–l**) Same as (**a–d**) but for precipitation and 850-hPa wind (m/s) based on ERA5 and PD, respectively


Precip and 850-hPa wind
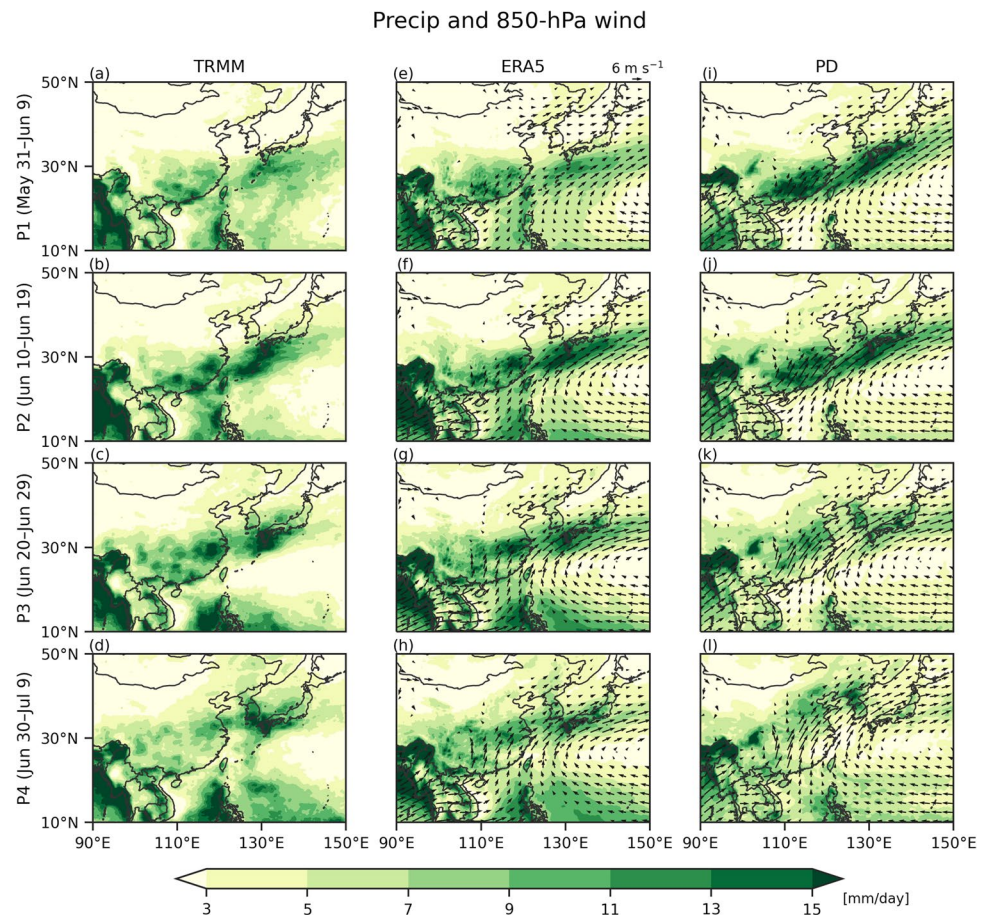
at the 1% level). The pattern of precipitation extremes overall follows the seasonal mean precipitation distribution (Fig. 4). There is a wide spread in the observed precipitation extremes, with TRMM as the highest and APHRODITE as the lowest in terms of intensity, consistent with Kim et al. (2019). Their differences can be more than 50 mm/day for the R99 values over the windward regions, such as the Bay of Bengal, the South China Sea, and the western tropical Pacific (Fig. 4e and f). Previous studies found that TRMM generally overestimates heavy precipitation (Zhao and Yatagai 2014) while APHRODITE underestimates the precipitation extremes (Lai et al. 2020). The simulated magnitude of precipitation extremes falls into the range of the observations (Fig. 4d and h). The R95 values in the PD simulation are near the lower bound of the observations (i.e., APHRODITE) while R99 is closer to the upper bound (i.e., TRMM). The pattern correlations between simulations and various observations are above 0.55 (significant at the 1% level), suggesting the model can reproduce well the synoptic features associated with the monsoon circulation. Overall, the high resolution PD simulation has a good fidelity of the monsoon precipitation and circulation on seasonal, intra-seasonal, and synoptic scales, which enables us to examine their responses to CO_2 forcing with more confidence.

3.2 EASM Responses to Global Warming

Figure 5 shows the responses of precipitation and the low-level circulation to doubling and quadrupling of the CO_2 concentration. In the following analysis, we also include the Indian monsoon region which shows a weaker monsoon circulation in responses to CO_2 forcing, consistent with a generally projected weakening of the global monsoon circulation (Wang et al. 2020). This weakening of the South Asian monsoon circulation due to CO_2 forcing mainly serves as a comparison to the enhancement of the EASM. By doubling the CO_2 concentration level, the circulation changes over the northern subtropics are characterized by anomalous anticyclonic circulation centered over southern India and the western Pacific and a trough centered at Indochina. This pattern weakens the climatological trough over eastern India while it reinforces the climatological southerly wind over East Asia, suggesting a weakened South Asian monsoon circulation and an enhanced EASM circulation. Under the influence of southwesterly oceanic flow, southwestern India and southern China experience a precipitation increase by about 20%. Moreover, the precipitation increases are on the northern side of the climatological rainfall band over eastern China, indicating a northward shift of the rainband

Fig. 3 The spatial distribution of 95th percentile of daily 2-m air temperature (K) in summer based on (**a**) APHRODITE, (**b**) ERA5, and (**c**) PD. (**d**–**f**) Same as (**a**–**c**) but for 99th percentile. The numbers in the parenthesis denote the pattern correlation between observations and PD
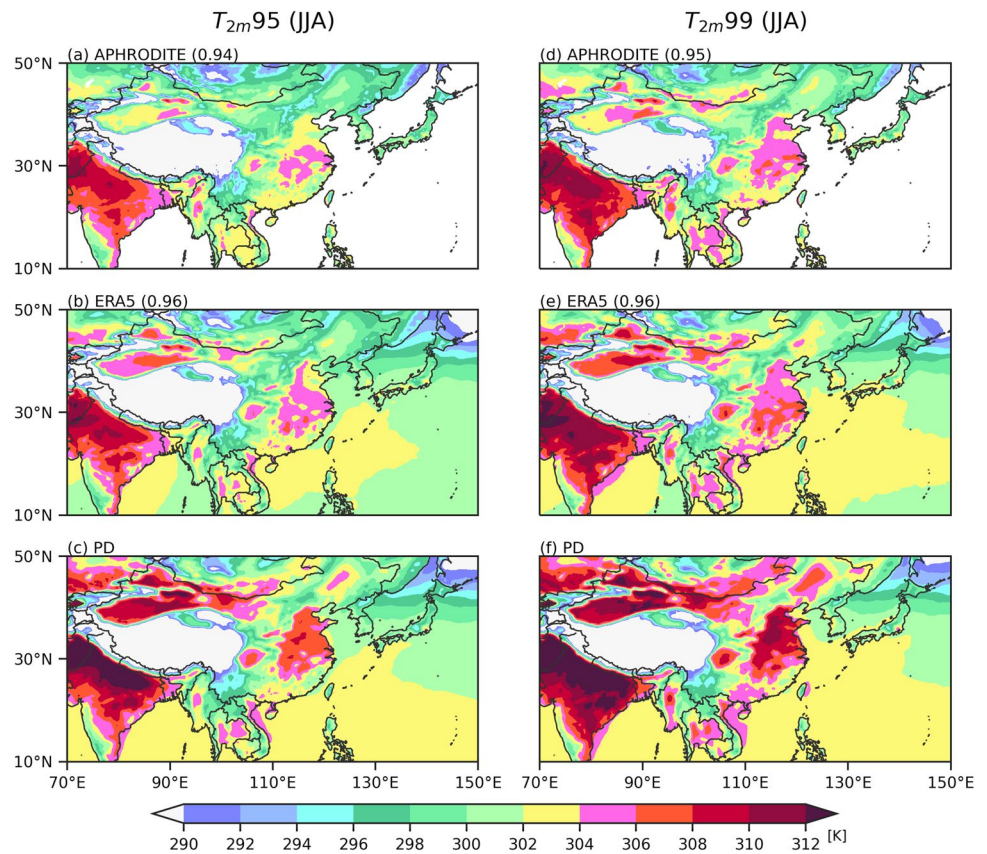
due to enhanced southerly anomalies (Fig. 1 and 5a). These anomalous southwesterly flows over western India and East Asia are mainly attributed to the CO_2-induced differential horizontal warming patterns manifested by a warmer Northern than Southern Hemisphere and warmer land than ocean (Lee and Wang 2014; Lau and Kim 2017; Wang et al. 2020). Consequently, there are anomalously strong cross-equatorial easterly flows over the southern Indian Ocean because of the interhemispheric temperature contrast, which then turn to southwesterlies towards the Indian subcontinent. Over East Asia, warmer land causes low-pressure anomalies to extend from eastern China to the northwestern Pacific across Korea and Japan (Fig. 6d). By contrast, relatively colder ocean-induced high-pressure anomalies appear over the western subtropical Pacific, showing a stronger WPSH in response to CO_2 forcing (Lee and Wang 2014). The sea-level pressure gradient between land and ocean leads to intensified southwesterly wind prevailing over the East China Sea and the northwestern Pacific (Fig. 5a). To the north, there is an anomalous cyclonic circulation centered over Japan in conjunction with the southward movement of the jet over the Pacific sector (Fig. 6a). Note the meridional shift of the jet stream due to greenhouse warming is of considerable uncertainty in climate models, mainly depending on the stratospheric cooling and Arctic surface warming (Shaw et al. 2016; Yim et al. 2016). In response to quadrupling the

CO_2 concentration, the overall patterns of changes in precipitation and low-level circulation are very similar to that induced by doubling CO_2, except that the magnitude is much larger, and more significant changes are shown (Fig. 5b). Larger interhemispheric temperature gradients and land-sea pressure gradients (Fig. 6h) lead to much stronger southerly wind anomalies over East Asia reaching northeastern China in comparison to south of 30°N in the $2 \times CO_2$ experiment. More moisture is transported to East China resulting in precipitation increases, showing an even stronger monsoon circulation in the $4 \times CO_2$ than the $2 \times CO_2$ simulation. Compared to $2 \times CO_2$, the jet stream is much weaker (Fig. 6a and e), which is also conducive to stronger low-level southerly wind anomalies. Note the increased precipitation is situated at the location of the climatological rainfall band over eastern China (Fig. 1 and 5b), suggesting an intensification in the $4 \times CO_2$ in contrast to a northward movement of Meiyu in the $2 \times CO_2$, albeit with stronger southerly winds in the former. This may indicate different mechanisms in driving the rainfall enhancement, which will be discussed below.

The enhanced moisture transport to inland areas and subsequent convergence can be induced by the increases in either convergence or specific humidity. To further understand their contributions to the precipitation increase over Asia, we analyze the moisture budget following Seager et al. (2010). The changes in MFC are further decomposed into

Fig. 4 Same as Fig. 3 but for precipitation
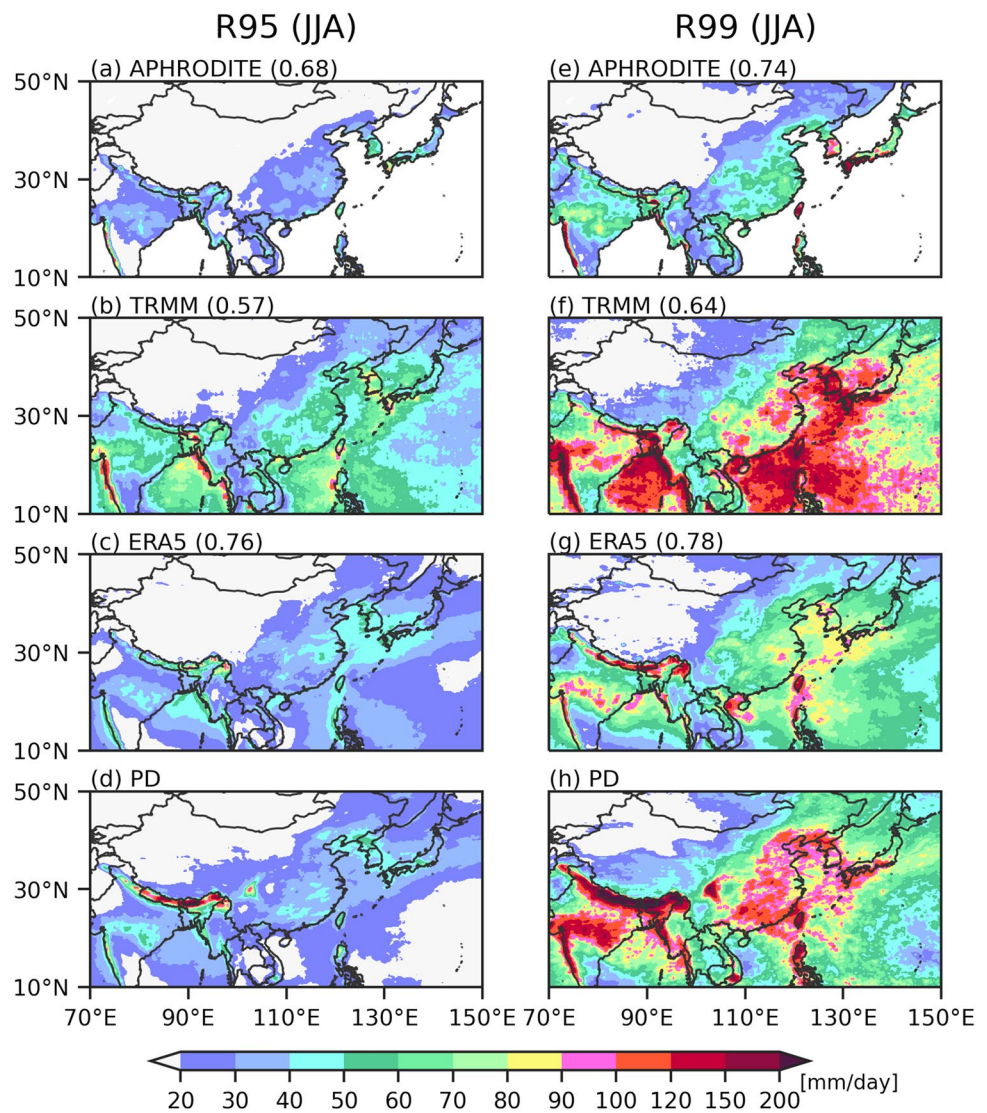
the monthly DY via circulation changes, the monthly TH via humidity changes, and the contribution from transient eddies on time scales less than a month as in previous studies (D'Agostino et al. 2019; Seager et al. 2010). The distribution of the P – E changes (Fig. 7a, e) is very similar to that of the precipitation changes (Fig. 5a, b), suggesting a minor role of evaporation changes. In response to doubling CO_2, there is a decrease of P – E over central India while at the same time there is an increase over southwestern India (Fig. 7a). This decrease over the core monsoon region is consistent with the low-level anticyclone (Fig. 5a) and downward motion anomalies (Fig. 6b). To the east, increased precipitation appears over Indochina and extends from South China to Japan across South Korea (Fig. 7a), corresponding to the anomalous trough over Indochina and intensified WPSH, respectively (Fig. 5a). Inspection of the decomposition shows that the pattern of P–E changes basically follows that of DY (Fig. 7a and b), indicating the vital

role of circulation changes in shaping the pattern of monsoon precipitation changes (Wang et al. 2020; Lau and Kim 2017). The general negative anomalies in DY (Fig. 7b) mean suppressed convection associated with low-level divergence. This enhanced divergence is mainly due to the increased atmospheric stability with more greenhouse gases (Fig. 6c), which has been discussed in previous studies (Wang et al. 2020; Lee and Wang 2014). An exception is southern China and mid-latitude inland regions where positive DY anomalies are presented corresponding to the intensified monsoon circulation due to the strengthened sea-level pressure gradient (Fig. 6d). Note the positive anomalies are in the north of the climatological rainband over eastern China, suggesting the driving role of DY in the northward shift of the rainband. Besides, the decreased low-level stability over land is also conducive to ascending anomalies and subsequent low-level convergence (Fig. 6c). The decreased stability due to increased CO_2 forcing is likely induced by the stronger
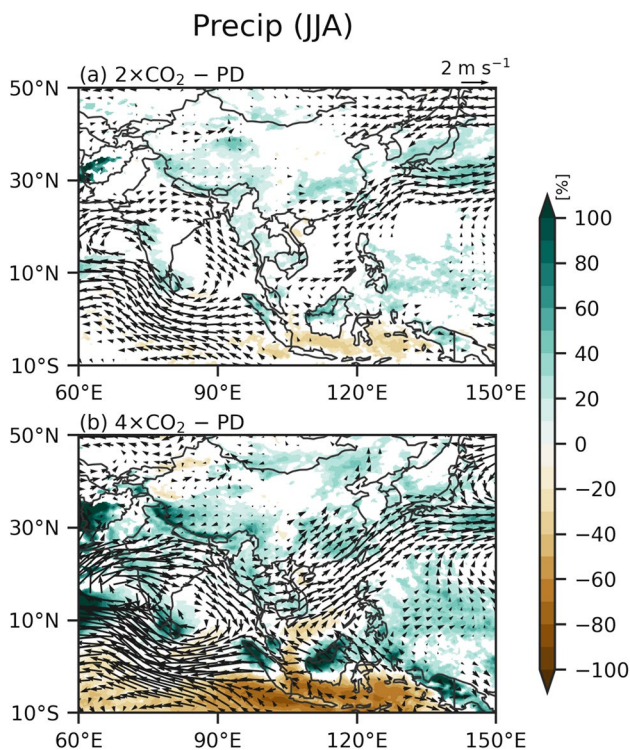
Precip (JJA)

Fig. 5 The spatial distribution of changes in precipitation (%) and 850-hPa wind (m/s) in summer between (**a**) $2\times CO_2$ simulation, (**b**) $4\times CO_2$ simulation and PD. Only changes at 0.05 significance level are presented according to the Student's t test. For wind, changes in either meridional or zonal component wind at 0.05 significance level are shown

low-level temperature increases over middle- to high-latitude inland areas in boreal summer (see Fig. 10a in Wang et al. 2020). TH generally contributes a relatively uniform pattern of positive anomaly (Fig. 7c) that mainly results from increased specific humidity as temperature increases (Held and Soden 2006). Over the core South Asian monsoon region, the wet anomalies due to TH only partially offset the contribution from DY, leading to dry anomalies there. In the main rainband of the EASM, those two components contribute to comparable wet anomalies. However, previous studies show more important DY effects than TH effects on the EASM precipitation (Oh et al. 2018; Li et al. 2019). Li et al. (2019) found that DY plays a dominant role for precipitation increase for a warming of 2–5 K above the pre-industrial global mean surface temperature. As warming level increases, DY can be two times of TH in generating positive precipitation anomalies. One possible reason accounting for the smaller contribution of DY in this study is the increased stability in the upper atmosphere in response to CO_2 forcing (Fig. S2), which can be measured by the temperature differences between 500 and 200 hPa. The increased upper atmospheric stability inhibits the ascending motion, deep convection, and subsequent low-level

convergence, thus reducing the DY contribution. Besides, the wide inter-model spread of responses to warming in DY and TH is found in the CMIP5 (IPCC, 2013) and CMIP6 models (Moon and Ha, 2020), which may also explain the relatively stronger TH contribution in this work. Interestingly, the pattern of contribution from transient eddies is opposite to that from DY, although its magnitude is much smaller (Fig. 7d). In the $4\times CO_2$ simulation, the pattern of sea-level pressure changes is very similar to the $2\times CO_2$ simulation but intensified by a factor of around 2 (Fig. 6d and h). Consequently, the circulation responses are enhanced, characterized by a stronger anticyclone over India and intensified southwesterly over East Asia. (Fig. 5b). The changes in DY are also stronger for $4\times CO_2$ than for $2\times CO_2$, but weaker in the rainband over East Asia (Fig. 7b and f). This is because the further enhancement of upper atmospheric stability (Fig. S2) suppresses the ascending anomalies and deep convections (Fig. 6f) and offsets the enhanced monsoon responses in $2\times CO_2$ although the lower atmosphere is more unstable over East Asia (Fig. 6g). By contrast, the enhanced upper atmospheric stability in $4\times CO_2$ reinforces the weakened monsoon responses in $2\times CO_2$ over the South Asian monsoon region. The weakened increase of the rainband due to DY over East Asia in $4\times CO_2$ than $2\times CO_2$ indicates that there is an optimal CO_2-induced warming level, which maximizes the influence of DY on precipitation increases over the monsoon front. Not surprisingly, the TH contribution further increases through humidity increases as a response to stronger warming for $4\times CO_2$ than $2\times CO_2$ (Fig. 7c and g). The precipitation increases due to TH outweigh the decreases caused by DY (Fig. 7f and g), leading to an overall increased precipitation over India for $4\times CO_2$ (Fig. 7e). Over China, TH accounts for more precipitation increases than DY (Fig. 7f and g), suggesting a dominant role of the former for $4\times CO_2$. The Meiyu band is intensified over eastern China mainly following TH changes in $4\times CO_2$ instead of shifting northward in $2\times CO_2$ because DY is suppressed due to further enhanced upper-atmospheric stability in $4\times CO_2$. We further decompose the DY term into advection and convergence components following Han et al. (2019). The advection changes between $4\times CO_2$ and $2\times CO_2$ show increases over the Meiyu band (Fig. S3b) in conjunction with the intensified southwesterly winds (Fig. 5). The decreased DY effects over eastern China is mainly driven by convergence changes (Fig. S3a) modulated by the strengthened upper atmospheric stability, indicating a coupled TH and DY impact through temperature changes.

The monsoon onset and withdrawal represent the start and end dates of the rainy season, respectively. Their predictions are crucial for agriculture and the economy over Asia but remain largely uncertain under global warming. Some studies suggest an earlier onset and later withdrawal of the EASM (Kitoh et al. 2013; Lee and Wang 2014) while other

Fig. 6 The spatial distribution of summer changes in (**a**) 300-hPa zonal wind (m/s), (**b**) 500-hPa vertical velocity (0.01 Pa/s), (**c**) temperature differences between 850 and 500 hPa (K), and (**d**) sea-level pressure (hPa) between $2\times CO_2$ and PD simulation. (**e–h**) Same as (**a–d**) but for $4\times CO_2$ simulation. Black dots represent the changes at 0.05 significance level. Blue contours in (**a**, **e**) denote the zonal wind climatology in PD. Red (blue) in (**b**, **f**) indicates descent (ascent)
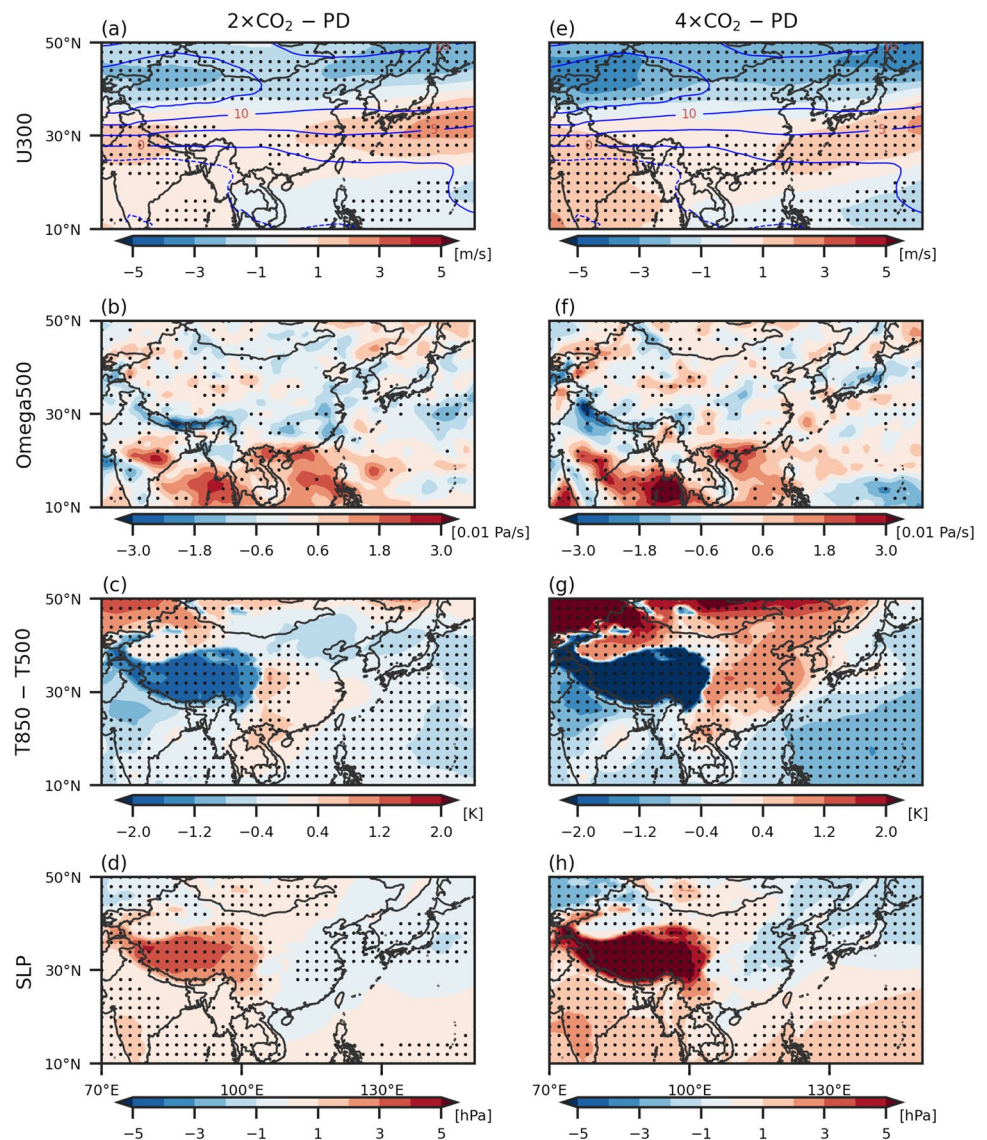
studies find a delayed onset and earlier withdrawal induced by the weakening of the upper-atmospheric meridional temperature gradient (Sabeerali and Ajayamohan 2018). The patterns of onset and retreat dates in PD are similar to those in previous studies using observations (Wang and Ho 2002; Dallmeyer et al., 2015), showing the model's capability in capturing the key monsoon evolution (Fig. 8a and d). In response to a doubling of the CO_2 concentration, the onset changes are characterized by a dipole pattern, with positive anomalies over South Asia (e.g., Indochina) and negative anomalies over East Asia and the western Pacific (Fig. 8b). This means a later onset in the former and an earlier onset in the latter. Increases of the withdrawal date are shown over the monsoon domain, indicating a late withdrawal (Fig. 8e). The larger increases of the withdrawal than onset date over India and surrounding oceanic areas suggest a longer rainy season there (Ha et al. 2020). By contrast, the

stronger positive anomalies of onset than withdrawal over Indochina mean a shorter rainy season there. Over East Asia, the lengthened rainy season is attributed to both the earlier onset and delayed withdrawal (Cui et al. 2020; Ha et al. 2020; Moon and Ha, 2020). The generally stronger responses of withdrawal than onset except over Indochina suggest its higher sensitivity to CO_2-induced warming so that the changes of the rainy season length are mainly driven by withdrawal changes. With quadrupling CO_2 forcing, the magnitudes of changes in both onset and withdrawal dates are more enhanced than those with doubling CO_2, particularly for withdrawal (Fig. 8c and f). Over the Yangtze River basin, the earlier onset (~4–6 pentads) and delayed withdrawal (~8–10 pentads) can prolong the monsoon season by more than 2 months. Note that only withdrawal changes over eastern China and the Arabian Sea in $4\times CO_2$ are shown as evidently significant with respect to their interannual

Fig. 7 The spatial distribution of summer changes (mm/day) in (**a**) precipitation minus evaporation (P – E), (**b**) dynamic term (DY), (**c**) thermo-dynamic term (TH), (**d**) transient term between 2×CO$_2$ simulation and PD. (**e–h**) Same as (**a–d**) but for 4×CO$_2$ simulation
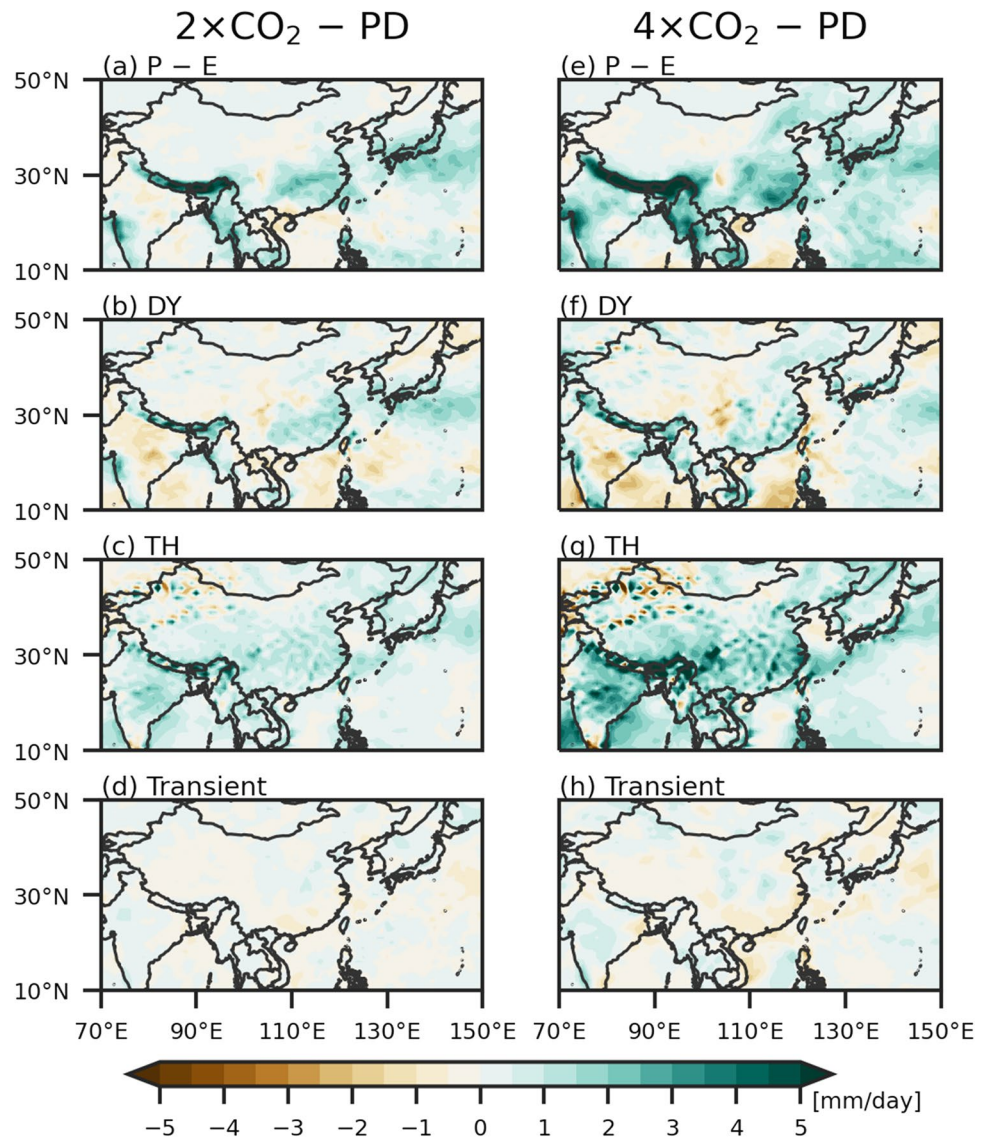
variability in PD. The interannual variations of onset and withdrawal dates are large, particularly in the latter (Fig. S4), which is likely because of the large variability of pentad precipitation (e.g., Montes et al., 2021). Interestingly, the duration of the monsoon season over Indochina becomes longer in 4×CO$_2$, in contrast to the shorter one in 2×CO$_2$ because of a more delayed retreat for 4×CO$_2$ concentration.

Climate extremes are projected to increase significantly under global warming over the Asian monsoon regions (Zhang and Zhou 2019; Kim and Bae 2020; Lee et al., 2021). Given its large population density, Asia is highly vulnerable to climate extremes (e.g., heatwaves and floods). However, regional projections of climate extremes are still rather uncertain in the latest climate models (Seneviratne and Hauser 2020), which may come from insufficient spatial resolution, particularly for precipitation extremes (van der Wiel et al., 2016; Iles et al. 2020). Table 1 shows

precipitation extremes pooled over six representative inland monsoon regions in response to CO$_2$ forcing.

The ranges of the R95 increases are from 1 to 32% for 2×CO$_2$ and from 16 to 40% for 4×CO$_2$, which are much wider than that for temperature (Table 1). The increases of R99 are generally larger than those of R95, suggesting that stronger precipitation extremes tend to be even stronger as CO$_2$ increases. This means a higher sensitivity of stronger precipitation extremes to CO$_2$ forcing. On average, the intensification of R95 over surface temperature changes is approximately 5%–6% K^{-1} while that of R99 is roughly 8% K^{-1}, with the Clausius-Clapeyron (CC) relation about 6.5% K^{-1} falling between both (Allen and Ingram 2002). This means that R95 is still not extreme enough to effectively consume all the atmospheric moisture to precipitate out as only the uppermost percentage of extreme changes follows the CC relation assuming marginal impact from

Fig. 8 The spatial distribution of monsoon onset date (pentad) (**a**) in PD, (**b**) changes between $2\times CO_2$ simulation and PD, and (**c**) changes between $4\times CO_2$ simulation and PD. (**d–f**) Same as (**a–c**) but for monsoon withdrawal date. Black dots denote the region where the responses are larger than one standard deviation of onset/withdrawal dates in the PD experiment
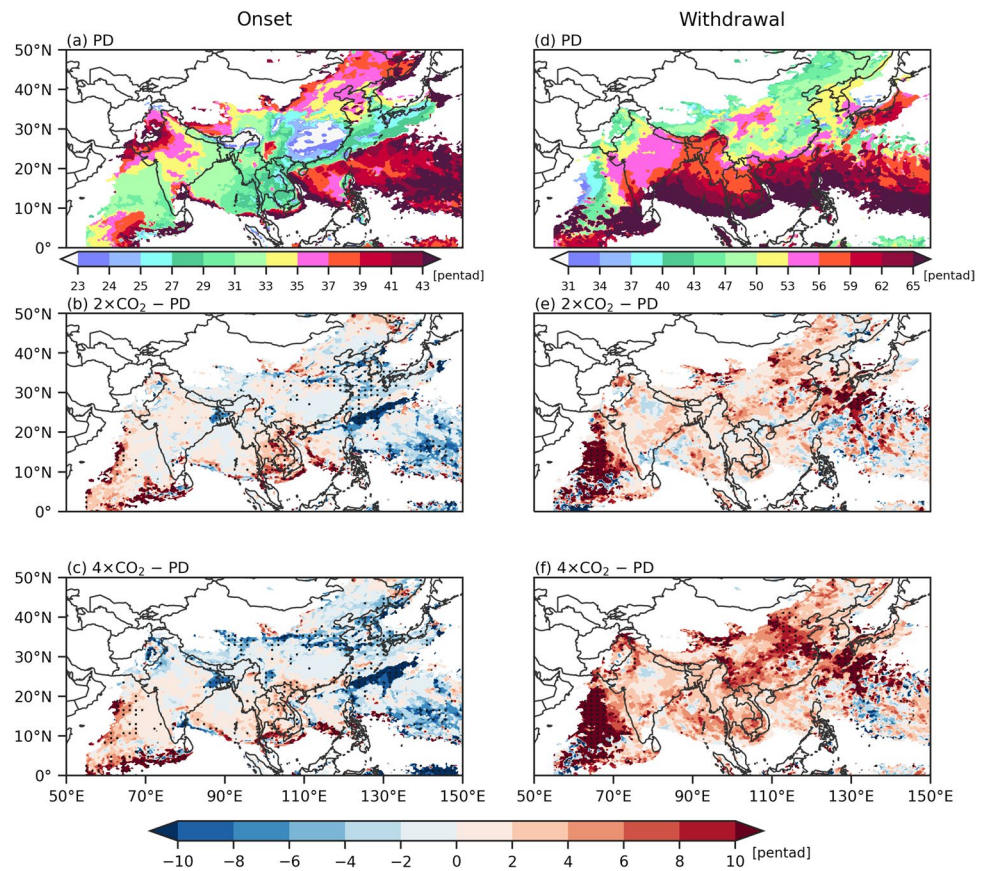

Table 1 The average of 95th and 99th percentile of near-surface air temperature (K) and precipitation (%) changes, and surface temperature (K) changes between $2\times CO_2$, $4\times CO_2$ and PD simulations over different land regions. Abbreviations: SC, South China; CEC, Central East China; NC, North China; KR, South Korea; JP, Japan; Avg: average over the all the monsoon subregions

		SC	CEC	NC	KR	JP	India	Avg
T95 (K)	$2\times CO_2$	3.4	4.7	3.9	3.1	2.4	3.0	3.4
	$4\times CO_2$	6.8	8.3	8.1	7.1	5.4	6.6	7.1
R95 (%)	$2\times CO_2$	20	32	1	17	23	13	18
	$4\times CO_2$	34	39	16	22	28	40	30
T99 (K)	$2\times CO_2$	3.7	4.7	4.2	3.3	2.4	2.9	3.5
	$4\times CO_2$	7.0	8.8	8.4	7.4	5.6	6.7	7.3
R99 (%)	$2\times CO_2$	26	31	12	22	26	23	23
	$4\times CO_2$	50	56	39	51	40	55	49
TS (K)	$2\times CO_2$	2.9	3.1	3.3	2.9	2.8	2.5	2.9
	$4\times CO_2$	6.2	6.7	7.0	6.7	6.4	5.6	6.4

circulation changes (Pall et al. 2007). By contrast, the super CC scaling of R99 is likely because the anomalous southerly winds bring more moisture via dynamical transport. Unlike the temperature extremes, the regional mean precipitation extreme increases do not scale with CO_2 concentration, which are on average below and above a factor of 2 for R95 and R99, respectively.

To determine whether precipitation extremes will increase significantly under CO_2-induced warming, the GPD is applied to model the tail of the precipitation distribution exceeding their 99.99[th] values (R99.99) at the present day

for each region. There are three parameters to determine the GPD: location, shape, and scale (Coles 2001). Larger values of scale and shape mean stronger extreme values, and the location parameter refers to the threshold above which the tail fits the GPD well. We choose R99.99 as the threshold because we cannot reject the GPD as the appropriate distribution of the precipitation data at the 1% significance level for all regions, particularly for larger regions with more samples. In this sense, Fig. 9 shows how intense precipitation extremes respond to CO_2 forcing. Error bars denote the standard deviations of the shape and scale parameters.

Korean Meteorological Society 🌏 Springer

Fig. 9 Shape (red) and scale (blue) parameters of generalized Pareto distribution fitting with 99.99th percentile of daily precipitation in PD, 2×CO$_2$, and 4×CO$_2$ over (**a**) South China, (**b**) Central East China, (**c**) North China, (**d**) South Korea, (**e**) Japan, and (**f**) India. Error bars represent one standard deviation
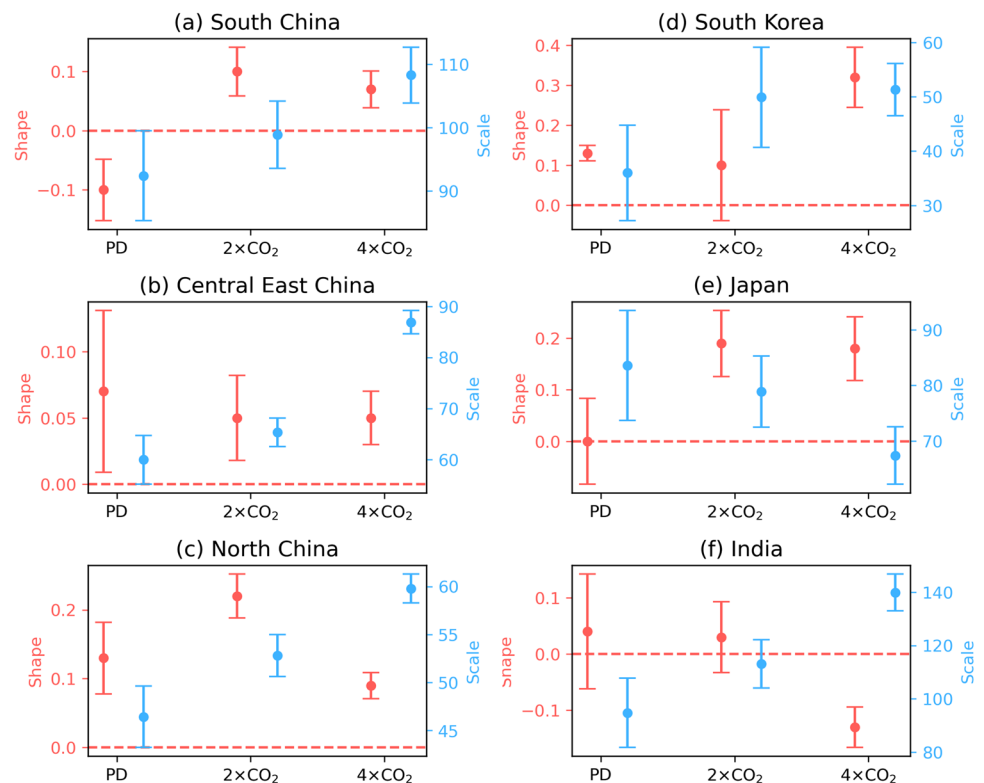
The shape parameters are larger in CO$_2$ perturbed simulations than PD over South China and Japan, suggesting significant increases in precipitation extremes. Similarly, the larger scale parameters over North China indicate stronger extremes there. Over South Korea and Central East China, the stronger precipitation extremes are only seen in 4×CO$_2$ but not for 2×CO$_2$. Over India, the scale parameter is larger in 4×CO$_2$ compared to PD, but the shape parameter is relatively smaller. Thus, there is apparent uncertainty whether R99.99 over India will significantly increase or not in response to 4×CO$_2$ forcing.

Besides precipitation, all the regions experience temperature increases of about 3.5 and 7.0 K on average in 2×CO$_2$ and 4×CO$_2$, respectively (Table 1). This means that the temperature increases over the monsoon domain roughly scale with the CO$_2$ concentration. The increase of T99 is slightly larger than that of T95, showing that stronger extremes warm more in response to CO$_2$ forcing (Duan et al. 2020). This conclusion is also confirmed by the probability density function of near-surface air temperature for each experiment (Fig. 10). The probability density differences among different experiments are significant at the 1% level according to the Kolmogorov–Smirnov test. In Fig. 10, the vertical dashed lines generally shift to the right faster than the vertical solid lines, indicating that T95 increases faster than the mode of the distribution. In other words, warmer temperatures warm more under CO$_2$-induced warming, which will increase the skewness of the temperature distribution. Besides, the mode

of the distribution decreases as CO$_2$ concentration increases, except over Japan, suggesting a wider temperature range with more CO$_2$. Note there is skewness in the distribution over South Korea and Japan, which is not present in the observations, implying model biases in reproducing temperature distribution over islands. This bias may be because the model cannot well simulate the anomalous advection of the stationary temperature gradient and the covariance between wind and temperature anomalies, which are critical for temperature skewness (Zhang et al. 2022). The underlying causes are unclear and beyond the scope of this study.

4 Conclusions and Discussion

In this study, we have assessed the performance of the EASM circulation and precipitation in one of the most finely resolved coupled global model simulations conducted so far, with horizontal resolutions of around 0.25° and 0.1° for the atmospheric and oceanic components, respectively. The PD simulation well replicates the spatial distribution and intensity of monsoon features on seasonal mean, intraseasonal, and synoptic scales albeit with overestimated southerly winds over East Asia. This stronger monsoon is accompanied by weaker subtropical westerly winds associated with dry biases over the western coast of Indochina and the Philippines, and stronger subtropical easterly winds associated with an excessive powerful WPSH. These biases

Fig. 10 The probability density function of daily 2-m air temperature (K) for summer in PD (black), $2\times CO_2$ (orange), and $4\times CO_2$ (red) over (**a**) South China (22°–28°N, 107.5°–122°E), (**b**) Central East China (28°–34°N, 107.5°–122°E), (**c**) North China (34°–43°N, 107.5°–122°E), (**d**) South Korea, (**e**) Japan, and (**f**) India. Only land grid points are considered. The vertical solid and dashed lines denote the mode and the 95th percentile of the distribution, respectively
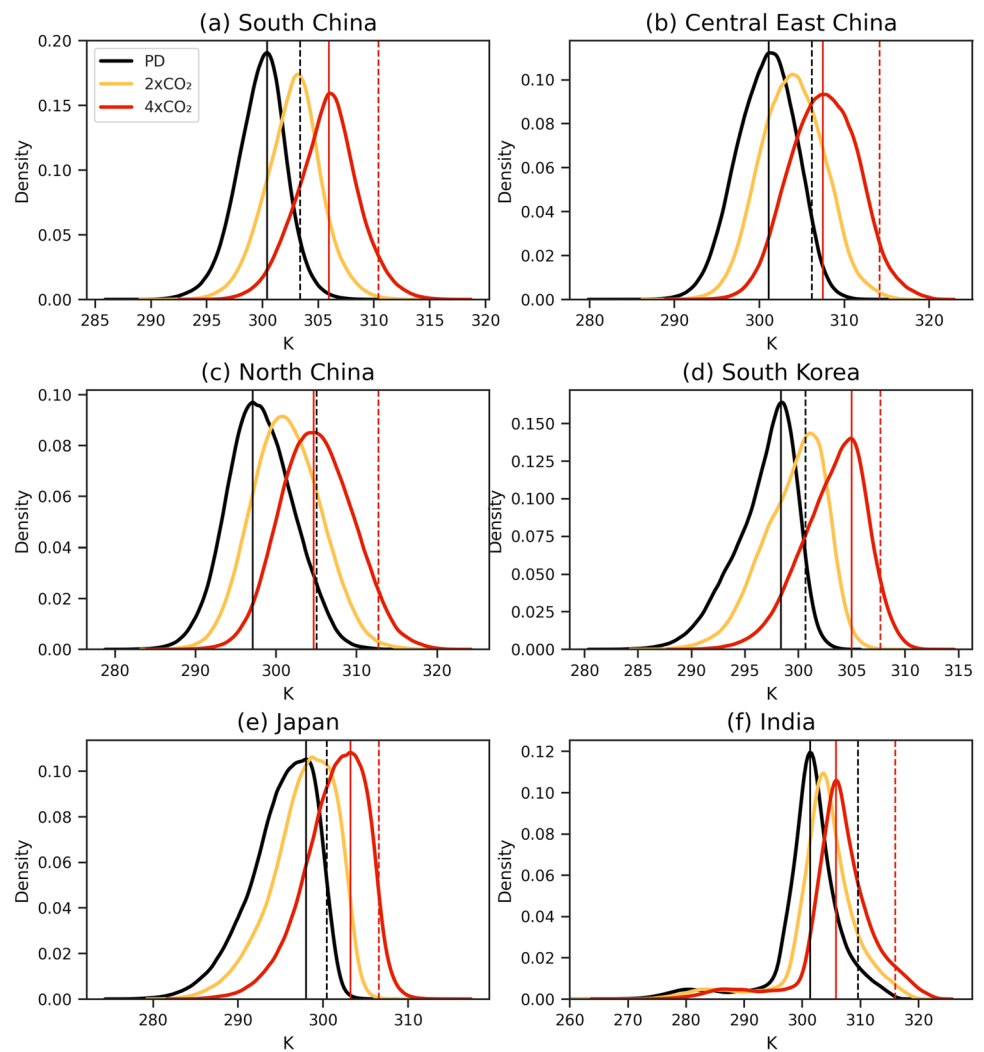
are possibly linked to local circulation errors associated with fast physical processes (e.g., convections and diurnal cycle) and unresolved terrain (Chen et al. 2019; Wu et al. 2014). Spatial resolutions higher than 25 km in atmospheric models may be needed to further improve the monsoon performance. Cloud resolving simulations may be essential to capture the coastal diurnal cycle and land-sea breeze associated with local complex terrain and convections over the Maritime Continent and the Indochina Peninsula (Oouchi et al. 2009; Li et al. 2020; Liu et al., 2021). A caveat is that increasing the horizontal resolution does not necessarily yield improved monsoon circulation and rainfall relative to observations (Lim et al. 2014). The model performance may be degraded as the convection schemes in many global coupled models are originally designed for relatively coarse resolutions (Wang et al. 2022). Thus, scale-aware parameterizations may be necessary and should be adjusted to match up with high resolution simulations (Johnson et al., 2016). The optimized horizontal resolution including relative importance of atmospheric and oceanic resolution (e.g.,

Sein et al., 2018; de la Vara et al., 2020; Jullien et al., 2020) for improving monsoon performance also warrants further investigation, which is beyond the scope of this study.

Additional CO_2 perturbed experiments, $2\times CO_2$ and $4\times CO_2$, have been analyzed in order to investigate the responses of the EASM to CO_2-induced warming by comparing with PD. In responses to doubling the CO_2 concentration, the EASM circulation is characterized by stronger southwesterly anomalies associated with the intensified WPSH (e.g., Zhou and Zou 2010; Dai et al. 2013; Endo et al., 2018) and an anomalous trough over Indochina. This finding is in contrast to a weakened circulation over most monsoon regions under global warming (IPCC, 2013; Li et al. 2019). By contrast, the South Asian monsoon is weakened, characterized by an anomalous anticyclone over the Indian subcontinent opposing to the climatological trough over eastern India. The anomalous southwesterly over northern Arabian Sea and southern China is mainly driven by the sea-level pressure gradient via the CO_2-induced warmer Northern Hemisphere than Southern Hemisphere

and warmer land than ocean, respectively. These anomalous flows bring abundant moisture to southwestern India and southern China, leading to precipitation increases there by 20%. Compared to doubling the CO_2 concentration, the patterns of changes in the monsoon circulation and precipitation are very similar in $4 \times CO_2$ but with a much stronger magnitude.

To disentangle the relative roles of circulation and humidity changes in driving monsoon precipitation anomalies due to CO_2 forcing, the MFC changes are decomposed into contributions from monthly DY and TH components and transient eddies on time scales less than a month. In $2 \times CO_2$, the changes of DY resemble those of P – E, suggesting its dominant role in shaping the precipitation responses (Wang et al. 2020; Lau and Kim 2017). The DY and TH components contribute to comparable wet anomalies of the rainband over East Asia, with marginal impact from transient eddies. In $4 \times CO_2$, TH outweighs DY, leading to general precipitation increases over the monsoon region. Compared to $2 \times CO_2$, the decreases in wet anomalies of the rainfall band due to DY is caused by the increased upper-atmospheric stability. This means that the CO_2-induced temperature changes can in turn modulate the circulation changes and subsequent DY effect, suggesting a coupling between the DY and TH components. Our decomposition of MFC cannot totally separate the contribution from circulation changes and temperature changes although this method initially is used to quantify the relative importance of circulation changes and humidity changes. One possible solution could be to conduct additional CO_2 experiments with the circulation constrained toward that in the PD experiment to disentangle the DY effects using a dynamical nudging method (e.g., Liu et al., 2021).

The monsoon season becomes longer over East Asia in response to doubling the CO_2 concentration due to the advanced onset and delayed withdrawal, particularly in the latter, consistent with previous studies (Lee and Wang 2014; Cui et al. 2020). This increased duration may be related to seasonal-mean precipitation increases under global warming (Goswami and Xavier 2005). The late withdrawal may be associated with higher mean sea-level pressure anomalies in the tropical western Pacific in favour of moisture transport to monsoon regions (Kitoh and Uchiyama 2006). The early onset is suggested to be linked to the convective activity over the tropical western Pacific (Jin and Stan 2019). In $4 \times CO_2$, the changes in onset and withdrawal dates are amplified, particularly in the latter, suggesting its higher sensitivity to CO_2 forcing. The monsoon duration can be longer by 2 months than that in PD over the Yangtze River basin.

For precipitation extremes, R95 increases at a rate of 5%–6% K^{-1} on average over the monsoon region while R99 increases at a larger rate of ~ 8% K^{-1}. The super CC scaling for R99 is mainly due to more oceanic moisture transport through anomalous southerly winds. On average, the precipitation extreme increases over the monsoon domain are not scaling with the CO_2 concentration levels, with a factor of below and above 2 for R95 and R99, respectively, from $2 \times CO_2$ to $4 \times CO_2$. Fitting the precipitation extremes exceeding the 99.99[th] percentile of PD with an extreme value distribution (i.e., GPD) shows significant increases over South China, North China, and Japan in CO_2 perturbed experiments, and over Central East China and South Korea in $4 \times CO_2$.

Note that the CO_2-perturbed simulations do not reach equilibrium completely as reflected by the long-term trend of global mean sea-surface temperature (Fig. S5). Thus, the results presented in this study combine both the fast (i.e., radiative forcing) and slow (i.e., sea-surface temperature) responses to CO_2 forcing. Previous studies revealed the competing effect of fast and slow responses in generating monsoon changes, which involves an enhancement associated with increased land-sea contrast in the former and a weakening accompanied with decreased land-sea contrast in the later (Shaw and Voigt 2015; Chen and Bordoni 2016). The intensified EASM indicates the dominant role of fast responses in our study. Disentangling the contributions of DY and TH in both fast and slow responses needs additional experiments forced by climatological SST as Chen and Bordoni (2016), which will be explored in future studies.

We acknowledge that the robustness of the findings needs to be assessed in other climate models. Nevertheless, this work serves as an example of how to evaluate the performance of monsoon circulation across different time scales in one of the highest resolution global coupled models. Understanding the responses of the EASM to different levels of CO_2 concentrations and the underlying physical mechanism can be beneficial to make better monsoon projection and mitigation strategy to future monsoon changes.

Declarations

Conflict of Interest The authors declare that they have no conflict of interest.

References

Allen, M.R., Ingram, W.J.: Constraints on future changes in climate and the hydrologic cycle. Nature **419**,(2002). https://doi.org/10.1038/nature01092

Boos, W.R., Hurley, J.V.: Thermodynamic bias in the multimodel mean boreal summer monsoon. J. Clim. **26**, 2279–2287 (2013). https://doi.org/10.1175/JCLI-D-12-00493.1

Coles, S.: An introduction to statistical modeling of extreme values (Vol. 208, p. 208). London: Springer (2001)

Chang, C.-P., Lu, M.-M., Lim, H.: Monsoon Convection in the Maritime Continent: Interaction of Large-Scale Motion and Complex Terrain. Meteorol. Monogr. **56**, 6.1-6.29 (2016). https://doi.org/10.1175/amsmonographs-d-15-0011.1

Chen, C.A., Hsu, H.H., Liang, H.C.: Evaluation and comparison of CMIP6 and CMIP5 model performance in simulating the seasonal extreme precipitation in the Western North Pacific and East Asia. Weather Clim. Extrem. **31**,(2021). https://doi.org/10.1016/j.wace.2021.100303

Chen, J., Bordoni, S.: Early summer response of the East Asian Summer Monsoon to atmospheric CO2 forcing and subsequent sea surface warming. J. Clim. (2016). https://doi.org/10.1175/JCLI-D-15-0649.1

Chen, W.T., Wu, C.M., Ma, H.Y.: Evaluating the bias of South China Sea summer monsoon precipitation associated with fast physical processes using a climate model hindcast approach. J. Clim. **32**, 4491–4507 (2019). https://doi.org/10.1175/JCLI-D-18-0660.1

Chen, X., Wu, P., Roberts, M.J., Zhou, T.: Potential underestimation of future Mei-Yu Rainfall with coarse-resolution climate models. J. Clim. **31**, 6711–6727 (2018). https://doi.org/10.1175/JCLI-D-17-0741.1

Chen, Y., Zhai, P.: Two types of typical circulation pattern for persistent extreme precipitation in Central-Eastern China. Q. J. R. Meteorol. Soc. **140**, 1467–1478 (2014). https://doi.org/10.1002/qj.2231

Chu, J.E., Wang, B., Lee, J.Y., Ha, K.J.: Boreal summer intraseasonal phases identified by nonlinear multivariate empirical orthogonal function-based self-organizing map (ESOM) analysis. J. Clim. **30**, 3513–3528 (2017). https://doi.org/10.1175/JCLI-D-16-0660.1

Chu, J.E., Lee, S.S., Timmermann, A., Wengel, C., Stuecker, M.F., Yamaguchi, R.: Reduced tropical cyclone densities and ocean effects due to anthropogenic greenhouse warming. Sci. Adv. **6**,(2020). https://doi.org/10.1126/sciadv.abd5109

Cui, J., Piao, S., Huntingford, C., Wang, X., Lian, X., Chevuturi, A., Turner, A.G., Kooperman, G.J.: Vegetation forcing modulates global land monsoon and water resources in a CO2-enriched climate. Nat. Commun. **11**,(2020). https://doi.org/10.1038/s41467-020-18992-7

D'Agostino, R., Bader, J., Bordoni, S., Ferreira, D., Jungclaus, J.: Northern Hemisphere Monsoon Response to Mid-Holocene Orbital Forcing and Greenhouse Gas-Induced Global Warming. Geophys. Res. Lett. **46**, 1591–1601 (2019). https://doi.org/10.1029/2018GL081589

Dai, A., Li, H., Sun, Y., Hong, L.C., Ho, L., Chou, C., Zhou, T.: The relative roles of upper and lower tropospheric thermal contrasts and tropical influences in driving Asian summer monsoons. J. Geophys. Res. Atmos. (2013). https://doi.org/10.1002/jgrd.50565

Dallmeyer, A., et al.: The evolution of sub-monsoon systems in the Afro-Asian monsoon region during the Holocene - Comparison of different transient climate model simulations. Clim. Past **11**, 305–326 (2015). https://doi.org/10.5194/cp-11-305-2015

de la Vara, A., Cabos, W., Sein, D.V., Sidorenko, D., Koldunov, N.V., Koseki, S., Soares, P.M.M., Danilov, S.: On the impact of atmospheric vs oceanic resolutions on the representation of the sea surface temperature in the South Eastern Tropical Atlantic. Clim. Dyn. (2020). https://doi.org/10.1007/s00382-020-05256-9

Ding, Y.: Summer monsoon rainfalls in China. J. Meteorol. Soc. Japan **70**, 373–396 (1992). https://doi.org/10.2151/jmsj1965.70.1B_373

Duan, S.Q., Findell, K.L., Wright, J.S.: Three Regimes of Temperature Distribution Change Over Dry Land, Moist Land, and Oceanic Surfaces. Geophys. Res. Lett. **47**,(2020). https://doi.org/10.1029/2020GL090997

Endo, H., A. Kitoh, and H. Ueda : A unique feature of the Asian summer monsoon response to global warming: The role of different land-sea thermal contrast change between the lower and upper troposphere. Sci. Online Lett. Atmos. (2018). https://doi.org/10.2151/SOLA.2018-010.

Fischer, E.M., Beyerle, U., Schleussner, C.F., King, A.D., Knutti, R.: Biased Estimates of Changes in Climate Extremes From Prescribed SST Simulations. Geophys. Res. Lett. **45**, 8500–8509 (2018). https://doi.org/10.1029/2018GL079176

Goswami, B.N., Xavier, P.K.: ENSO control on the south Asian monsoon through the length of the rainy season. Geophys. Res. Lett. **32**, 1–4 (2005). https://doi.org/10.1029/2005GL023216

Ha, K.J., Moon, S., Timmermann, A., Kim, D.: Future Changes of Summer Monsoon Characteristics and Evaporative Demand Over Asia in CMIP6 Simulations. Geophys. Res. Lett. **47**,(2020). https://doi.org/10.1029/2020GL087492

Han, Z., Su, T., Zhang, Q., Wen, Q., Feng, G.: Thermodynamic and dynamic effects of increased moisture sources over the Tropical Indian Ocean in recent decades. Clim. Dyn. (2019). https://doi.org/10.1007/s00382-019-04977-w

Held, I.M., Soden, B.J.: Robust responses of the hydrological cycle to global warming. J. Clim. **19**, 5686–5699 (2006). https://doi.org/10.1175/JCLI3990.1

Hersbach, H., et al.: The ERA5 global reanalysis. Q. J. R. Meteorol. Soc. **146**, 1999–2049 (2020). https://doi.org/10.1002/qj.3803

Huang, D.Q., Zhu, J., Zhang, Y.C., Huang, A.N.: Uncertainties on the simulated summer precipitation over Eastern China from the CMIP5 models. J. Geophys. Res. Atmos. **118**, 9035–9047 (2013). https://doi.org/10.1002/jgrd.50695

Huang, L., Lee, S.S., Timmermann, A.: Caspian Sea and Black Sea Response to Greenhouse Warming in a High-Resolution Global Climate Model. Geophys. Res. Lett. **48**,(2021). https://doi.org/10.1029/2020GL090270

Huffman, G.J., et al.: The TRMM Multisatellite Precipitation Analysis (TMPA): Quasi-global, multiyear, combined-sensor precipitation estimates at fine scales. J. Hydrometeorol. **8**, 38–55 (2007). https://doi.org/10.1175/JHM560.1

Iles, C.E., Vautard, R., Strachan, J., Joussaume, S., Eggen, B.R., Hewitt, C.D.: The benefits of increasing resolution in global and regional climate simulations for European climate extremes. Geosci. Model Dev. **13**, 5583–5607 (2020). https://doi.org/10.5194/gmd-13-5583-2020

IPCC: Climate Change 2013: The Physical Science Basis. Contribution of Working Group I to the Fifth Assessment Report of the Intergovernmental Panel on Climate Change. Ipcc **5**, 1535 (2013). https://doi.org/10.1017/CBO9781107415324

Jin, Y., Stan, C.: Changes of East Asian summer monsoon due to tropical air-sea interactions induced by a global warming scenario. Clim. Change (2019). https://doi.org/10.1007/s10584-019-02396-8

Johnson, S. J., et al.: The resolution sensitivity of the South Asian monsoon and Indo-Pacific in a global 0.35° AGCM. Clim. Dyn. (2016). https://doi.org/10.1007/s00382-015-2614-1

Jullien, S., Masson, S., Oerder, V., Samson, G., Colas, F., Renault, L.: Impact of ocean-atmosphere current feedback on ocean mesoscale activity: Regional variations and sensitivity to model resolution. J. Clim. (2020). https://doi.org/10.1175/JCLI-D-19-0484.1

Kim, I.W., Oh, J., Woo, S., Kripalani, R.H.: Evaluation of precipitation extremes over the Asian domain: observation and modelling studies. Clim. Dyn. 52, 1317–1342 (2019). https://doi.org/10.1007/s00382-018-4193-4

Kim, J.B., Bae, D.H.: Intensification characteristics of hydroclimatic extremes in the Asian monsoon region under 1.5 and 2.0°C of global warming. Hydrol. Earth Syst. Sci. 24, 5799–5820 (2020). https://doi.org/10.5194/hess-24-5799-2020

Kim, T., Lee, S., Park, H.J., Cha, D.H., Seo, K.H.: The impact of coupled air–sea interaction on extreme East Asian summer monsoon simulation in CMIP5 models. Int. J. Climatol. 41, 6336–6349 (2021). https://doi.org/10.1002/joc.7198

Kitoh, A., Uchiyama, T.: Changes in onset and withdrawal of the East Asian summer rainy season by multi-model global warming experiments. J. Meteorol. Soc. Japan (2006). https://doi.org/10.2151/jmsj.84.247

Kitoh, A., Kusunoki, S.: East Asian summer monsoon simulation by a 20-km mesh AGCM. Clim. Dynam. 31, 389–401 (2008)

Kitoh, A., Endo, H., Krishna Kumar, K., Cavalcanti, I.F.A., Goswami, P., Zhou, T.: Monsoons in a changing world: A regional perspective in a global context. J. Geophys. Res. Atmos. 118, 3053–3065 (2013). https://doi.org/10.1002/jgrd.50258

Lai, S., Xie, Z., Bueh, C., Gong, Y.: Fidelity of the APHRODITE Dataset in Representing Extreme Precipitation over Central Asia. Adv. Atmos. Sci. 37, 1405–1416 (2020). https://doi.org/10.1007/s00376-020-0098-3

Lau, N.C., Ploshay, J.J.: Simulation of synoptic- and subsynoptic-scale phenomena associated with the East Asian summer monsoon using a high-resolution GCM. Mon. Weather Rev. 137, 137–160 (2009). https://doi.org/10.1175/2008MWR2511.1

Lau, W.K.M., Kim, K.M.: Competing influences of greenhouse warming and aerosols on Asian summer monsoon circulation and rainfall. Asia-Pacific J. Atmos. Sci. 53, 181–194 (2017). https://doi.org/10.1007/s13143-017-0033-4

Lee, J.-Y., et al.: Future Global Climate: Scenario-Based Projections and Near-Term Information. Climate Change 2021: The Physical Science Basis. Contribution of Working Group I to the Sixth Assessment Report of the Intergovernmental Panel on Climate Change, p. 195 (2021)

Lee, J.Y., Wang, B.: Future change of global monsoon in the CMIP5. Clim. Dyn. 42, 101–119 (2014). https://doi.org/10.1007/s00382-012-1564-0

Lee, J.Y., Wang, B., Seo, K.H., Ha, K.J., Kitoh, A., Liu, J.: Effects of mountain uplift on global monsoon precipitation. Asia-Pacific J. Atmos. Sci. 51, 275–290 (2015). https://doi.org/10.1007/s13143-015-0077-2

Lee, J.Y., et al.: The long-term variability of Changma in the East Asian summer monsoon system: A review and revisit. Asia-Pacific J. Atmos. Sci. 53, 257–272 (2017). https://doi.org/10.1007/s13143-017-0032-5

Li, P., Furtado, K., Zhou, T., Chen, H., Li, J., Guo, Z., Xiao, C.: The diurnal cycle of East Asian summer monsoon precipitation simulated by the Met Office Unified Model at convection-permitting scales. Clim. Dyn. (2020). https://doi.org/10.1007/s00382-018-4368-z

Li, Z., Sun, Y., Li, T., Ding, Y., Hu, T.: Future Changes in East Asian Summer Monsoon Circulation and Precipitation Under 1.5 to 5 °C of Warming. Earth's Futur. 7, 1391–1406 (2019). https://doi.org/10.1029/2019EF001276

Lim, K.S.S., Hong, S.Y., Yoon, J.H., Han, J.: Simulation of the summer monsoon rainfall over East Asia using the NCEP GFS cumulus parameterization at different horizontal resolutions. Weather Forecast. (2014). https://doi.org/10.1175/WAF-D-13-00143.1

Liu, Z., M. A. Bollasina, L. J. Wilcox, J. M. Rodríguez, and L. A. Regayre: Contrasting the Role of Regional and Remote Circulation in Driving Asian Monsoon Biases in MetUM GA7.1. J. Geophys. Res. Atmos., 126 (2021). https://doi.org/10.1029/2020JD034342.

Luo, M., Lau, N.C.: Heat waves in southern China: Synoptic behavior, long-term change, and urbanization effects. J. Clim. 30, 703–720 (2017). https://doi.org/10.1175/JCLI-D-16-0269.1

Montes, C., N. Acharya, M. A. Stiller-Reeve, C. Kelley, and S. M. Q. Hassan: Interannual variability of monsoon onset and withdrawal in Bangladesh. Atmos. Sci. Lett. (2021). https://doi.org/10.1002/asl.1069.

Moon, S., and K. J. Ha: Future changes in monsoon duration and precipitation using CMIP6. NPJ Clim. Atmos. Sci., 3 (2020). https://doi.org/10.1038/s41612-020-00151-w.

Oh, H., Ha, K.J.: Role of the surface boundary conditions in boreal spring on the interannual variability of the multistage evolution of the East Asian summer monsoon. J. Clim. 33, 1845–1861 (2020). https://doi.org/10.1175/JCLI-D-19-0249.1

Oh, H., Ha, K.J., Timmermann, A.: Disentangling Impacts of Dynamic and Thermodynamic Components on Late Summer Rainfall Anomalies in East Asia. J. Geophys. Res. Atmos. 123, 8623–8633 (2018). https://doi.org/10.1029/2018JD028652

Oouchi, K., Noda, A.T., Satoh, M., Wang, B., Xie, S.P., Takahashi, H.G., Yasunari, T.: Asian summer monsoon simulated by a global cloud-system-resolving model: Diurnal to intra-seasonal variability. Geophys. Res. Lett. (2009). https://doi.org/10.1029/2009GL038271

Palazzi, E., von Hardenberg, J., Terzago, S., Provenzale, A.: Precipitation in the Karakoram-Himalaya: a CMIP5 view. Clim. Dyn. 45, 21–45 (2015). https://doi.org/10.1007/s00382-014-2341-z

Pall, P., Allen, M.R., Stone, D.A.: Testing the Clausius-Clapeyron constraint on changes in extreme precipitation under CO_2 warming. Clim. Dyn. 28, 351–363 (2007). https://doi.org/10.1007/s00382-006-0180-2

Sabeerali, C.T., Ajayamohan, R.S.: On the shortening of Indian summer monsoon season in a warming scenario. Clim. Dyn. 50, 1609–1624 (2018). https://doi.org/10.1007/s00382-017-3709-7

Seager, R., Naik, N., Vecchi, G.A.: Thermodynamic and dynamic mechanisms for large-scale changes in the hydrological cycle in response to global warming. J. Clim. 23, 4651–4668 (2010). https://doi.org/10.1175/2010JCLI3655.1

Sein, D. V., et al.: The Relative Influence of Atmospheric and Oceanic Model Resolution on the Circulation of the North Atlantic Ocean in a Coupled Climate Model. J. Adv. Model. Earth Syst. (2018). https://doi.org/10.1029/2018MS001327

Seneviratne, S.I., Hauser, M.: Regional Climate Sensitivity of Climate Extremes in CMIP6 Versus CMIP5 Multimodel Ensembles. Earth's Futur. 8,(2020). https://doi.org/10.1029/2019EF001474

Seo, K. H., J. Ok, J. H. Son, and D. H. Cha: Assessing future changes in the East Asian summer monsoon using CMIP5 coupled models. J. Clim. (2013). https://doi.org/10.1175/JCLI-D-12-00694.1

Shaw, T. A., and A. Voigt: Tug of war on summertime circulation between radiative forcing and sea surface warming. Nat. Geosci. (2015). https://doi.org/10.1038/ngeo2449

Shaw, T.A., et al.: Storm track processes and the opposing influences of climate change. Nat. Geosci. **9**, 656–664 (2016). https://doi.org/10.1038/ngeo2783

Small, R. J., et al.: A new synoptic scale resolving global climate simulation using the Community Earth System Model. J. Adv. Model. Earth Syst. (2014). https://doi.org/10.1002/2014MS000363

Son, J.H., Seo, K.H.: East Asian summer monsoon precipitation response to variations in upstream westerly wind. Clim. Dyn. **1**, 1–8 (2022). https://doi.org/10.1007/S00382-021-06117-9/FIGURES/7

Son, J.H., Seo, K.H., Wang, B.: Dynamical Control of the Tibetan Plateau on the East Asian Summer Monsoon. Geophys. Res. Lett. (2019). https://doi.org/10.1029/2019GL083104

Son, J.H., Seo, K.H., Wang, B.: How Does the Tibetan Plateau Dynamically Affect Downstream Monsoon Precipitation? Geophys. Res. Lett. **47**, e2020GL090543 (2020). https://doi.org/10.1029/2020GL090543

Sperber, K.R., Annamalai, H., Kang, I.S., Kitoh, A., Moise, A., Turner, A., Wang, B., Zhou, T.: The Asian summer monsoon: An intercomparison of CMIP5 vs. CMIP3 simulations of the late 20th century. Clim. Dyn. **41**, 2711–2744 (2013). https://doi.org/10.1007/s00382-012-1607-6

Wang, B., Ho, L.: Rainy season of the Asian-Pacific summer monsoon. J. Clim. **15**, 386–398 (2002). https://doi.org/10.1175/1520-0442(2002)015%3c0386:RSOTAP%3e2.0.CO;2

Wang, B., Ding, Q., Fu, X., Kang, I.S., Jin, K., Shukla, J., Doblas-Reyes, F.: Fundamental challenge in simulation and prediction of summer monsoon rainfall. Geophys. Res. Lett. **32**,(2005). https://doi.org/10.1029/2005GL022734

Wang, B., Jin, C., Liu, J.: Understanding Future Change of Global Monsoons Projected by CMIP6 Models. J. Clim. **33**, 6471–6489 (2020). https://doi.org/10.1175/JCLI-D-19-0993.1

Wang, X., Zhang, G.J., Wang, Y.: Evaluating and Improving Scale-Awareness of a Convective Parameterization Closure Using Cloud-Resolving Model Simulations of Convection. J. Geophys. Res. Atmos. (2022). https://doi.org/10.1029/2021JD035729

van der Wiel, K., et al.: The resolution dependence of contiguous U.S. precipitation extremes in response to CO2 forcing. J. Clim. **29**, 7991–8012 (2016). https://doi.org/10.1175/JCLI-D-16-0307.1

Wilcox, L.J., Dong, B., Sutton, R.T., Highwood, E.J.: The 2014 hot, dry summer in northeast Asia. Bull. Am. Meteorol. Soc. **96**, S105–S110 (2015). https://doi.org/10.1175/BAMS-D-15-00123.1

Wilcox, L. J., et al.: Accelerated increases in global and Asian summer monsoon precipitation from future aerosol reductions. Atmos. Chem. Phys. (2020) 10.5194/acp-20-11955-2020

Wu, C.H., Hsu, H.H., Chou, M.D.: Effect of the Arakan Mountains in the northwestern Indochina Peninsula on the late May Asian monsoon transition. J. Geophys. Res. **119**, 10769–10779 (2014). https://doi.org/10.1002/2014JD022024

Xin, X., Wu, T., Zhang, J., Yao, J., Fang, Y.: Comparison of CMIP6 and CMIP5 simulations of precipitation in China and the East Asian summer monsoon. Int. J. Climatol. **40**, 6423–6440 (2020). https://doi.org/10.1002/joc.6590

Yamanaka, M. D., S. Y. Ogino, P. M. Wu, H. Jun-Ichi, S. Mori, J. Matsumoto, and F. Syamsudin: Maritime continent coastlines controlling Earth's climate. Prog. Earth Planet. Sci. (2018). https://doi.org/10.1186/s40645-018-0174-9.

Yao, J., Zhou, T., Guo, Z., Chen, X., Zou, L., Sun, Y.: Improved performance of high-resolution atmospheric models in simulating the East Asian summer monsoon rain belt. J. Clim. **30**, 8825–8840 (2017). https://doi.org/10.1175/JCLI-D-16-0372.1

Yatagai, A., Kamiguchi, K., Arakawa, O., Hamada, A., Yasutomi, N., Kitoh, A.: Aphrodite constructing a long-term daily gridded precipitation dataset for Asia based on a dense network of rain gauges. Bull. Am. Meteorol. Soc. **93**, 1401–1415 (2012). https://doi.org/10.1175/BAMS-D-11-00122.1

Yim, B.Y., Min, H.S., Kug, J.S.: Inter-model diversity in jet stream changes and its relation to Arctic climate in CMIP5. Clim. Dyn. **47**, 235–248 (2016). https://doi.org/10.1007/s00382-015-2833-5

Zhang, B., Linz, M., Chen, G.: Interpreting Observed Temperature Probability Distributions Using a Relationship between Temperature and Temperature Advection. J. Clim. **35**, 705–724 (2022). https://doi.org/10.1175/JCLI-D-20-0920.1

Zhang, W., Zhou, T.: Significant increases in extreme precipitation and the associations with global warming over the global land monsoon regions. J. Clim. **32**, 8465–8488 (2019). https://doi.org/10.1175/JCLI-D-18-0662.1

Zhao, T., Yatagai, A.: Evaluation of TRMM 3B42 product using a new gauge-based analysis of daily precipitation over China. Int. J. Climatol. **34**, 2749–2762 (2014). https://doi.org/10.1002/joc.3872

Zhou, S., Huang, G., Huang, P.: Changes in the East Asian summer monsoon rainfall under global warming: moisture budget decompositions and the sources of uncertainty. Clim. Dyn. **51**, 1363–1373 (2018). https://doi.org/10.1007/s00382-017-3959-4

Zhou, T., Zou, L.: Understanding the predictability of East Asian summer monsoon from the reproduction of land-sea thermal contrast change in AMIP-type simulation. J. Clim. (2010). https://doi.org/10.1175/2010JCLI3546.1

Zhou, T., Zou, L.: Understanding a hot summer in central eastern China: summer 2013 in context of multimodel trend analysis. Bull. Am. Meteorol. Soc. **95**, S54–S57 (2014)

Zhou, T., Song, F., Lin, R., Chen, X., Chen, X.: The 2012 North China Floods: Explaining an extreme rainfall event in the context of a longer-term drying Tendency. Bull. Am. Meteorol. Soc. **94**, S49–S51 (2013)

Zou, L., Zhou, T.: Asian summer monsoon onset in simulations and CMIP5 projections using four Chinese climate models. Adv. Atmos. Sci. **32**, 794–806 (2015). https://doi.org/10.1007/s00376-014-4053-z